Aerodynamic levitator furnace for measuring thermophysical properties of refractory liquids

Langstaff, David Philip; Gunn, Matthew David; Greaves, George Neville; Marsing, Andreas; Kargl, Florian

Published in:
Review of Scientific Instruments

DOI:
10.1063/1.4832115

Publication date:
2013

Citation for published version (APA):
Langstaff, D. P., Gunn, M. D., Greaves, G. N., Marsing, A., & Kargl, F. (2013). Aerodynamic levitator furnace for measuring thermophysical properties of refractory liquids. *Review of Scientific Instruments*, *84*(12), Article 124901. https://doi.org/10.1063/1.4832115

AIP | Review of Scientific Instruments

Aerodynamic levitator furnace for measuring thermophysical properties of refractory liquids

D. Langstaff, M. Gunn, G. N. Greaves, A. Marsing, and F. Kargl

Citation: Rev. Sci. Instrum. **84**, 124901 (2013); doi: 10.1063/1.4832115
View online: http://dx.doi.org/10.1063/1.4832115
View Table of Contents: http://rsi.aip.org/resource/1/RSINAK/v84/i12
Published by the AIP Publishing LLC.

Aerodynamic levitator furnace for measuring thermophysical properties of refractory liquids

D. Langstaff,[1] M. Gunn,[1] G. N. Greaves,[1,a)] A. Marsing,[2,b)] and F. Kargl[2,c)]
[1]*Centre for Advanced Functional Materials and Devices, Institute of Mathematics and Physics, Aberystwyth University, Aberystwyth SY23 3BZ, United Kingdom*
[2]*Institut für Materialphysik im Weltraum, Deutsches Zentrum für Luft- und Raumfahrt (DLR), 51170 Köln, Germany*

(Received 20 August 2013; accepted 5 November 2013; published online 5 December 2013)

The development of novel contactless aerodynamic laser heated levitation techniques is reported that enable thermophysical properties of refractory liquids to be measured *in situ* in the solid, liquid, and supercooled liquid state and demonstrated here for alumina. Starting with polished crystalline ruby spheres, we show how, by accurately measuring the changing radius, the known density in the solid state can be reproduced from room temperature to the melting point at 2323 K. Once molten, by coupling the floating liquid drop to acoustic oscillations via the levitating gas, the mechanical resonance and damping of the liquid can be measured precisely with high-speed high-resolution shadow cast imaging. The resonance frequency relates to the surface tension, the decay constant to the viscosity, and the ellipsoidal size and shape of the levitating drop to the density. This unique instrumentation enables these related thermophysical properties to be recorded *in situ* over the entire liquid and supercooled range of alumina, from the boiling point at 3240 K, until spontaneous crystallization occurs around 1860 K, almost 500 below the melting point. We believe that the utility that this unique instrumentation provides will be applicable to studying these important properties in many other high temperature liquids. © *2013 AIP Publishing LLC*. [http://dx.doi.org/10.1063/1.4832115]

I. INTRODUCTION

Accurate knowledge of thermophysical properties is important for fundamental studies of phase transformations, nucleation, and more generally the simulation of material production routes such as casting, glass formation, and ceramic processes. The more conventional methods of measuring density, surface tension, and viscosity of metallic and oxide liquids are very often hampered by melt-container interactions and sometimes the elevated temperatures involved in measuring refractories at the melting point or above. Moreover, reaching supercooled conditions, on the large scale relevant for materials processing at elevated temperatures, is generally precluded by heterogeneous nucleation at the container wall on laboratory scales. Containerless handling of liquids can provide unique solutions. Indeed, measurements of thermophysical properties using contactless liquid processing methods have been successfully carried out employing electromagnetic levitation (EML),[1–5] electrostatic levitation (ESL),[6–8] to a less extent gas-film levitation (GFL)[9–11] and acoustic levitation (AL) with the sample contained by a surrounding liquid[12] or freely suspended in a gaseous environment,[13–15] and very recently also conical-nozzle aerodynamic levitation (ADL).[16] In case of AL, ESL, and GFL drops are mechanically excited by oscillating the levitation forces. For EML, this is only possible in a controlled way under microgravity conditions. For ADL, the droplet was so far self-excited through the levitation force. By contrast to the single study of thermophysical properties,[16] ADL has been more widely used in conjunction with synchrotron radiation, neutron and NMR techniques.[17–26] In this study, large discrepancies of over an order of magnitude were found between containerless measurements of thermophysical properties of Al_2O_3 and earlier work using conventional container and rheological techniques. Moreover, the supercooled region has remained unexplored. Where changes in thermophysical properties with temperature are comparatively small above the melting point in classical liquids, for supercooled liquids below the liquidus, densities, for instance, can change by tens of % and viscosities by many decades, particularly when the liquids are fragile.[27]

Using EML, microgravity conditions can provide accurate results of viscosity for metallic samples,[28,29] whereas ground-based measurements that are generally more conveniently carried out, can also give accurate results for density and surface tension[1] even for a deformed drop. Whereas the determination of density works more or less well with all of the mentioned methods (EML, ESL, GFL, AL, ADL), the determination of surface tension and viscosity is not straight forward. It varies between materials and levitation techniques. For example, viscosity EML measurements are hampered by electromagnetic stirring forces related to heating and levitation and the tear-like shape of droplets.[1,30,31] For ESL, where heating is separate from levitation, metals can be studied at lower temperatures. In this case, drops are almost spherical and viscosity measurements easier but the charged surface may also impact on the determined surface tension and viscosity.[32] Also high vacuum conditions are generally used

a)Also at Department of Materials Science and Metallurgy, University of Cambridge, Cambridge BB2 3QZ, United Kingdom.
b)Also at Fachbereich Physik, Universität Konstanz, 78457 Konstanz, Germany.
c)Electronic mail: florian.kargl@dlr.de. Also at Centre for Advanced Functional Materials and Devices, Institute of Mathematics and Physics, Aberystwyth University, Aberystwyth SY23 3BZ, United Kingdom.

which can lead to unpredictable charge-loss for oxides as well as loss of sample material[33,34] compared with a hybrid ESL-ADL working under pressure.[35] AL, on the other hand, has been used for liquids at ambient temperature conditions and below as well as for metal liquids with a low melting point like Indium.[12] Investigations of high-melting point materials are currently still lacking. Similar to ESL and different to EML and ADL for AL, the sample is fully visible. However, the samples are typically deformed by the acoustic force showing oblate or prolate shape. As shown for EML also for AL droplet shape will have an impact on thermophysical property measurements as discussed in Ref. 13 as might have the interaction of the levitation force with the sample driving fluid-flow inside of the sample.[14,36] Different to the other techniques AL also enables to measure viscosities exceeding 10^2 Pa s exciting forced rotation in the sample as demonstrated by Ohsaka *et al.*[15] However, this technique relies on a relaxation model to interpret the measured data. By comparison, ADL has often proved the method of choice for studying oxide liquids. Using a conical nozzle[19,20,23,37–40] drops are melted by laser heating as shown in Figure 1. Experiments, however, have so far focused on structure and dynamics on the microscopic scale.[18,20,21,23,26] Of the few thermophysical property measurements reported, for GFL the droplet is severely distorted from a spherical shape,[10,11] making the determination of surface tension and viscosity far from ideal.[9] For ADL (cf. Figure 1), near-spherical droplet conditions can often be achieved by optimizing weight with surface tension. Previous work determining viscosity and surface tension,[16,41] however, relied on self-excitation from sporadic oscillations resulting from the tumbling motion of the droplet within the nozzle. Resonance patterns had relatively poor statistics compared to forced oscillations with EML and ESL methods. Moreover, viscosity was necessarily estimated from the width of the power spectrum rather than from decay constants when forced oscillations are released for which sampling statistics are superior.

In this paper, we present a novel laser-heated ADL furnace for thermophysical property measurements on refractory liquids – though ADL is not restricted to only this class of materials – based on the oscillating-droplet technique. Forced oscillations are excited acoustically for the near-spherical droplet transmitted through the levitation gas and, unlike EML and AL, are effectively decoupled from the levitation forces. Compared to EML, heating is independent of levitation and compared to ESL measurements are made at ambient pressure and are not vulnerable to the interaction between the charged surface and the electrostatic levitation field. However, the gas flow around the sample could – similar to the levitation force in AL – potentially cause flow within the sample impacting on the viscosity measurement. In this paper, the potential using ADL for characterizing the thermophysical properties of supercooled liquid oxides *in situ* at ultra-high temperatures and in the supercooled region below the melting point is demonstrated. High speed video imaging, using shadow casting with a source brighter than the incandescent drop, has been developed to measure density from the radius of spherical solids and from the size and shape of levitated droplets during heating or free-cooling. This is demonstrated

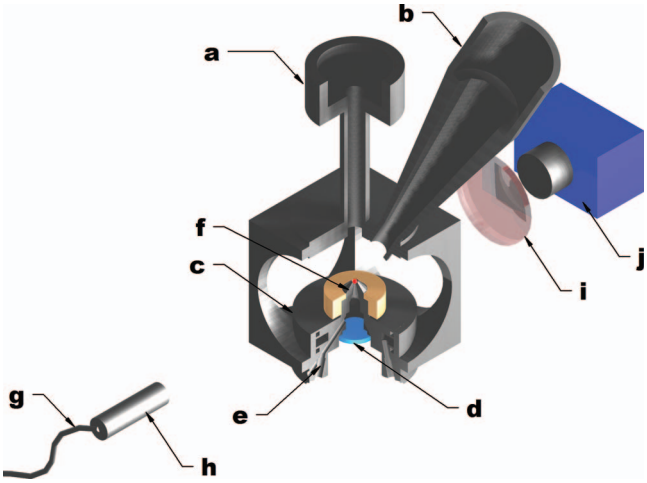

FIG. 1. Levitation process chamber. Constructed around a ThorLabs 60 mm optical cube: (a) top laser port, (b) pyrometer head inclined ∼30° from the vertical, (c) water-cooled levitation stage, (d) ZnSe/NaCl window (transparent to 10.59 μm) separating the levitation gas from the bottom laser port, (e) inlet for levitation gas, (f) aerodynamic conical converging-diverging levitator nozzle (30° inlet – 60° outlet) with a central opening of 1.2 mm in diameter and depth chosen so that a 2 mm sphere in rest position is visible above the rim of the nozzle by about 0.2 mm, (g) back lighting fiber-coupled laser source (200 mW, 660 nm MRL-III CNI), (h) beam expanding optics delivering an approximately 11 mm diameter beam at the sample, (i) visible light bandpass filter with 10 nm (FWHM) centered around 660 nm, and (j) high-speed camera (800 fps) for shadow casting of the levitated drop equipped with a telecentric lens – Sill Optics S5LPJ9325 with 5× magnification at a working distance of 69 mm. The other side ports can be used for synchrotron small and wide angle scattering experiments similar to previous experiments.[23]

for alumina between room temperature, the melting point at 2323 K, and the boiling point at 3240 K. By pulsing the gas stream in the supercooled and liquid states, the surface tension and viscosity are obtained by analyzing backlighted images of the time-dependent amplitude of resonant mechanical vibrations and during resonant decay, respectively. Moreover, this very compact furnace can also be used with synchrotron radiation equipment for additional *in situ* small and wide angle scattering experiments similar to previous experiments (cf. Ref. 23).

The paper begins with a description of the construction and organization of the ADL furnace, the laser optics, pyrometer, and gas supply (cf. Sec. II A), followed by ADL furnace control including recording of temperature and levitation control (cf. Sec. II B), *in situ* imaging under stable and pulsed gas conditions, including melting of polished ruby spheres and during free-cooling of alumina from the boiling point (cf. Sec. II C), as well as acoustic shape excitations (cf. Sec. II D). It is then shown how these are incorporated into the measurement of thermophysical properties of liquid and supercooled alumina (cf. Sec. III), demonstrating the major improvements in precision and versatility that can now be achieved in measuring the liquids thermophysical properties.

II. TECHNICAL ASPECTS

A. Furnace construction

The ADL furnace setup (cf. Figure 2) consists of a CO_2 laser system providing two times up to 125 W laser power

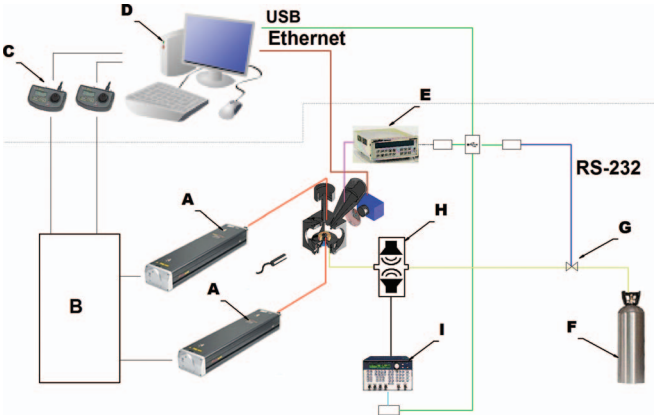

FIG. 2. Schematics of levitation furnace instrumentation. Heating facilitated by two 125 W CO_2 SynRAD Evolution Series 10.59 μm lasers (A) placed on top of each other with a 190 mm separation. Laser power output from RF-3000 laser power supply (B) controlled by SynRAD UC-2000 units (C), and in turn by 0-10 V D/A outputs from a NuDaq PC1-9112 card in the control computer (D) which allows for easy override in case of software failure. Contained laser beams are directed and focused by gold-plated copper 25 mm mirrors mounted on ThorLabs KCB1 right angle kinematic mounts adjusted by micrometer screws which deliver focused beams at the sample stage of ~0.8 mm in diameter. Temperature is measured with a Luxtron Accufiber M10 (E) using a HF 950 nm high temperature head. Levitation gas (F) flow to the process chamber (cf. Fig. 1) is controlled by a Brooks MFC 5850S mass flow controller (G). Mechanical excitation of the levitated drop is facilitated by two Visaton FRS5 50 mm 8 loudspeakers (H) fed by a power amplifier and a Thurlby-Thandar Instruments TG1304 frequency generator (I). *In situ* imaging of the levitating oscillating drop is obtained by high speed camera: Vision Research Phantom V7.1 (Aberystwyth) or Mikrotron MotionBlitz EOS Cube6 (DLR) (J).

to the sample and operating at a wavelength of 10.59 μm for heating and melting, which is ideal for oxide systems that strongly absorb at this wavelength, and a sample process chamber (cf. Figure 1), which houses facilities for levitation and acoustic excitation, temperature measurement, and sample monitoring. The lasers are mounted on top of each other for compactness and the two beams are guided towards the process chamber via flat and focusing mirrors which deliver a beam of about 0.8 mm in diameter to the sample position. The entire laser beampath is fully enclosed and the laser power supply is interlocked to the access ports of the process chamber, as are the laser shutters. Finally, the laboratory access doors are also wired into the lock-up circuit to achieve laser class 1 status, which reduces occupational hazards for bench-top operation and is compatible with equipment at large scale facilities.

The process chamber (cf. Figure 1) has six ports. The bottom opening contains the levitator stage. Sample temperature control, and sample position and shape monitoring, including sample illumination for inspection, are admitted at the top. The chamber's side ports are available for specifically designed windows. The two heating laser beams enter the chamber from the top (a) and bottom (d), the latter being directed through the water-cooled aluminum cylinder of the levitation stage (c), which is also equipped with a port for the levitation gas (e). The gas enters the pre-chamber before being directed to the conical levitation nozzle shaped so that the center of the levitated drop is proud of the rim (f). The bottom of the pre-chamber is sealed with an infrared-transparent window to accommodate the lower laser beam. Mechanical excitation of the levitated drops is activated by an acoustic oscillator system (cf. Figure 2), consisting of two loudspeakers mounted either side of a small aluminum chamber aligned perpendicular to the gas stream. These are connected via a power amplifier to a function generator, which sets the amplitude and waveshape of the stimulating waveform. Sample temperatures are measured using a single-color pyrometer bolted to the top port of the process chamber. The temperatures are read into the computer system by using an A/D-converter connected to the analogue output of the Luxtron M10 pyrometer control. High-speed cameras are used to measure droplet size and shape horizontally (cf. Figure 2). A telecentric lens with a pupil entrance at infinity at a magnification 5× is used. The magnification of the lens is independent of the sample distance or position in the field of view. Backlighting for shadow casting is enabled using a fiber-coupled diode laser (g) with a beam expanding optics opposite the high speed camera (h). For synchrotron radiation experiments, the X-ray beam can intersect the specimen through the ports through 25 μm thick X-ray grade clear ruby MICA windows at right angles to (g) with detectors for small and wide angle scattering located downstream.

B. Control

The levitator furnace is controlled via three independent LabView control interfaces all running simultaneously on a single PC. The mass flow controller interface sets the gas flow in 1% steps and reads back at 10 Hz intervals. The power for the top and bottom laser is controlled via the second interface. This interface enables pre-defined heating and cooling profiles to be executed as well as rapid quenching of the sample for free-cooling experiments. It also records the pyrometer temperatures at rates of up to 100 Hz. The final interface controls the frequency for video imaging and can be adapted for different high speed cameras.

C. Imaging and image analysis

For liquid oxides, the emissivity is typically greater than 0.8 within the camera wavelength range. With incandescence at high temperatures sample self-illumination can be a first approach and has previously been employed by other groups using aerodynamic levitation techniques.[16,34,41,42] In order to make measurements over the extensive temperature ranges described here, shadow-cast imaging, like used in the past for EML work,[43] of the levitating drop is essential. Here, the camera and lens configuration do not have to be adapted for different experimental conditions. Generally, sharp sample edges can be imaged only if the aperture of the telecentric lens is closed as much as possible, compatible with the dynamic range for the shutter speed, once the frame rate is set. Typical frame rate settings are 800 fps.

Recorded images are analyzed using our own interface written in LabView. The surface profile of the partially visible droplet is determined using an edge detection algorithm. Horizontal and vertical radii, the droplet center position, and

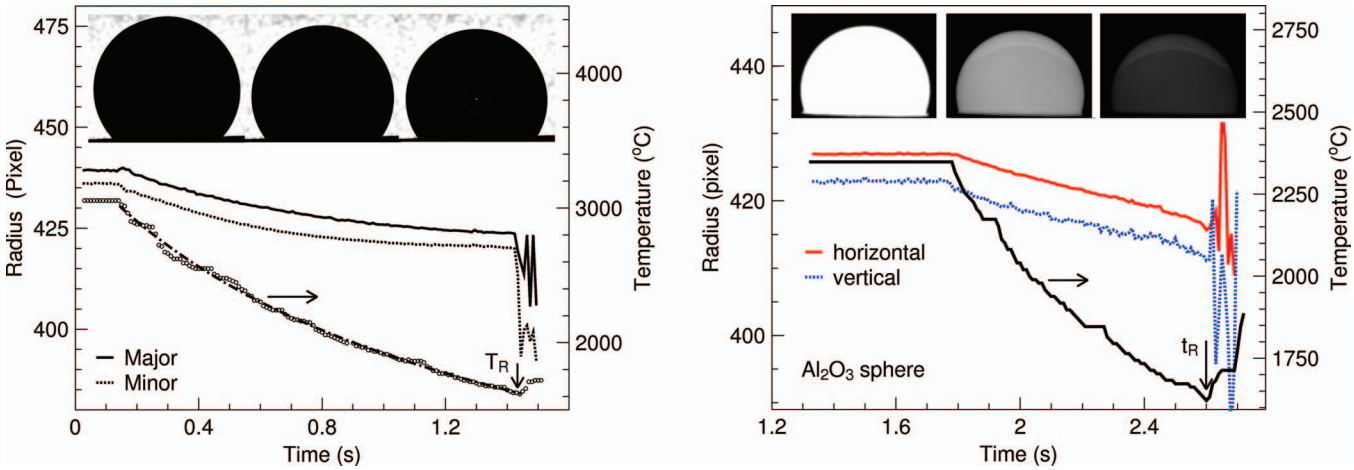

FIG. 3. Size and shape of aerodynamically levitated liquid alumina obtained from free cooling (black line), contrasting backlighted imaging for drops quenched from 2977 °C (left) with incandescent imaging quenched from 2350 °C (right). Horizontal r_h (red dotted line) and vertical r_v (dashed blue line) radii obtained from image analysis as a function of time together with the corresponding temperatures. The shadow cast images (left) and the self-illuminated images (right) show the droplet shortly before quenching, halfway through, and at the final stage (left to right) as before recalescence sets in by t_R around 1600 °C.

the sample area are determined frame by frame fitting an ellipse shape to the surface profile. For sample edge detection, three parameters can be varied: steepness, width, and contrast. This enables to determine the absolute sample radius to two pixels or less (cf. Appendix C for further details). At low temperatures and during free-cooling density runs, sample self-illumination becomes a limit and can lead to an apparent reduction in the absolute droplet diameter, and hence, to an overestimation of sample density. Back-lighting with a cold light source and suitable filters minimizes this problem. However, care has to be taken at the highest temperatures if incandescence becomes comparable in intensity. This limit was not reached here, even when temperatures reached the boiling point of alumina, due to the use of a high intensity visible light laser source and a narrow band optical filter.

Density measurements can be optimally obtained by imaging the droplet under free-cooling, where the sample temperature is homogeneous at elevated temperatures and cooling almost entirely radiative (cf. Figure 3). The high-speed camera images the vertical and horizontal radii from which the volume can be estimated, assuming an ellipsoid shape, with the temperature obtained pyrometrically. Relying on self-illumination, with the brightness reducing sharply as the temperature falls, the measured radii can be affected for incandescent imaging. Accordingly, large temperature ranges necessitate cooling with several different shutter speeds, which may disturb sample-radius determination. These anomalies can be virtually eliminated if back lighting is used.

D. Acoustic excitation

Different waveforms and symmetries for acoustic excitation can be selected by the frequency generator. For the present experiments, a conventional sine wave was employed as this proved to be the most effective way to excite droplet oscillations in a predictable way. The optimum sample amplitude gave a maximum deviation in sphere width of between 2% and 5% of its nominal diameter, ensuring that the sample oscillations approximated to the simple harmonic oscillator equation.

1. Resonant surface oscillations

The squares of the resonant frequencies of an oscillating sphere are proportional to its surface tension γ[44]

$$\gamma = \frac{3\pi \nu_R^2 M}{l(l-1)(l+2)}, \tag{1}$$

where M is the mass, ν_R the resonance frequency, and l describes the oscillation mode. Typically, the $l = 2$ mode is dominant, in which case

$$\gamma = \frac{3}{8}\pi \nu_R^2 M. \tag{2}$$

With asphericity and rotational motion the $l = 2$ mode is split into five modes ($l = 2$, $m = 0, \pm 1, \pm 2$) which can all be observed,[45] with a sum rule correlating the measured resonance frequencies with the surface tension.[46] This requires the forces on the surface of the levitated sphere to be estimated which are not readily available for ADL. The sum rule resulting from calculations for EML setups indicate that the correction to surface tension is about 20% compared to just using the ($l = 2$, $m = 0$)-mode frequency.

In order to determine γ for an aerodynamically levitated droplet, the resonance frequencies also have to be determined. Compared to EML where the oscillations on the droplet surface are self-excited due to interaction with the electromagnetic field, in ADL, if the droplet is levitated stably, surface oscillations are absent. Even when it is levitated unstably, surface oscillations have significantly smaller amplitudes than for EML leading to larger fluctuations in the Fourier spectra.[41] In order to obtain surface oscillations for ADL with reproducible strength, the droplet needs to be forced to oscillate and the Fourier amplitude obtained. By sweeping through a range of frequencies with high-speed camera imaging, a resonance spectrum can be obtained from which the ($l = 2$, m

$= 0, \pm 1, \pm 2$)-mode frequencies can be determined. The primary resonant frequency ($l = 2$, $m = 0$), where vertical and horizontal motion are phase shifted by 90°, can often be recognized by eye.

2. Damping constant

For a spherical sample, viscosity η is related to the damping constant Γ of the resonant surface oscillations.[47] For the $l = 2$ mode,

$$\Gamma = \frac{20\pi R}{3M}\eta = \frac{5}{\rho R^2}\eta\,, \tag{3}$$

where R is the radius of the oscillating sphere, M its mass, and ρ its density. To determine Γ, the droplet is excited for a few seconds close to the primary resonance frequency ($l = 2$, $m = 0$), the excitation removed, and the decay of the oscillation amplitude monitored. Images are then analyzed for horizontal and vertical radii, r_h and r_v, respectively, and fit in a two stage process. Assuming simple harmonic oscillator motion for the steady state

$$r_{h/v}(t) = A \cdot \sin[2\pi \nu_{ho}(t - t_0)] + r_0\,, \tag{4}$$

where A is the amplitude, ν_{ho} the excitation frequency, r_0 the mean sample radius, and t_0 an offset. For the damped decay,

$$r_{h/v}(t) = A \cdot \exp[-\Gamma(t - t_1)] \cdot \sin[2\pi \nu_{dho}(t - t_0)] + R_{av}\,. \tag{5}$$

A is the same constant as in Eq. (4) and kept constant, ν_{dho} gives the resonance frequency for the droplet, R_{av} is the radius of the droplet in rest, and t_1 is the time the decay starts. As ν_{dho} is the primary resonance frequency of the droplet, this can be used in Eq. (2) to estimate the corresponding surface tension γ.

III. THERMOPHYSICAL PROPERTY RESULTS AND DISCUSSION

A. Shape and size of liquid drops

Following calibration of the high speed camera (see Appendix B), temperature dependent densities of alumina were determined under free-cooling conditions. Figure 3 shows the droplet radii r_h and r_v matched to the changing temperature during cooling to the onset of recalescence t_R, under incandescent (right) and under back lighted conditions (left). Images of the levitated sphere are also included at spot temperatures. Taken together they clearly show the advantages of using a shadow casting geometry for determining droplet size, compared to relying on incandescence light levels. This image is also far sharper with backlighting and highlights how incandescent images underestimate sample size by ≈2 %. This worsens at lower temperatures, and overall leads to significant overestimation of density.

B. Density

Figure 4 depicts the density of a single crystal of ruby during heating (left) using shadow-casting and the resulting variation in density of liquid alumina during free cooling (right) for both types of imaging. This is calculated as $3M/(4\pi\, r_M^2 r_m)$, whereby r_M and r_m are half the major and minor axis, respectively, assuming the sample is symmetric about the minor axis. On the left the density of a polished spherical ruby crystal is shown using back lighting, heated from ambient through the melting point T_m. The major and minor axes are equal until T_m is approached, where they separate as the shape changes from spherical to ellipsoidal. While the density of the solid falls monotonically from room temperature as the temperature rises, following a linear thermal expansion coefficient of $\alpha = 7.0 \times 10^{-6}$ K^{-1} corresponding well to literature values, it drops sharply by 24% to about 2.9 g cm^{-3} at the liquidus. This large density change corresponds to the atomic structure altering from corundum, where

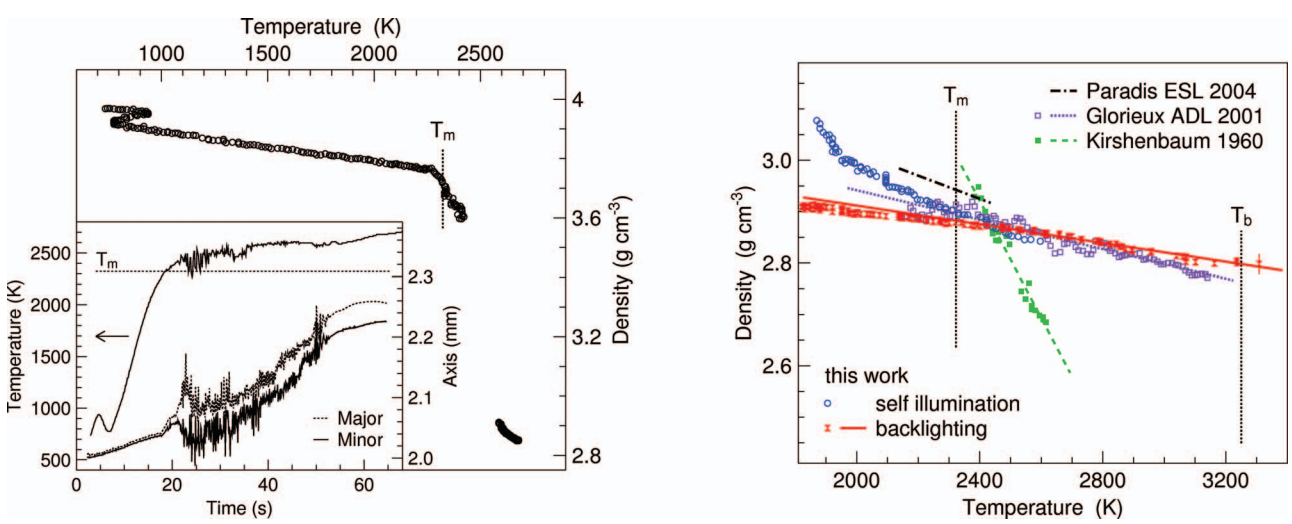

FIG. 4. (Left) Density of ruby heated from room temperature to the melting point $T_m = 2323$ K. (Right) Density of a liquid alumina droplet cooled from the boiling point $T_b = 3240$ K to recalescence under supercooling $T_R = 1863$ K. Earlier work with aerodynamically levitated samples[16] and electrostatically levitated samples[33] are included. For previous ADL data, no account was taken of asphericity as only r_h was measured. Work on alumina using conventional methods (triangles and solid line)[48] show the greatest disparity with contactless methods. The considerable scatter is attributed to variable processing conditions.

the coordination of aluminum is octahedral and of oxygen is 4-fold, to that of the liquid alumina,[18] where aluminum is mainly 4- and 5-fold coordinated with oxygen occupying 2- and 3-fold sites.[20] The particular proportions of multiple configurations have been determined by computer modeling of the structure factor in the liquid state, and are dependent on the density chosen.[20,26]

Turning now to cooling the liquid through to the supercooled state, the density on free cooling measured with shadow casting extends the temperatures accessed up to the boiling point T_b of alumina (3240 K). On cooling, the liquid drop supercools ~400°, before recrystallizing at the recalescence temperature T_R (~1900 K). Above the melting temperature the linear thermal expansion coefficient of liquid alumina $\alpha = 1.0 \times 10^{-5}\,\mathrm{K}^{-1}$, much higher than that of values reported in literature for solid alumina, reflects the substantial difference in the atomic structure between solid and liquid state.[20,26]

The underestimation of the size of liquid drops with incandescent imaging, especially at lower temperatures, is also exacerbated by the need to limit the temperature range for a fixed shutter time is a known phenomenon. Moreover, we found that merging several cooling runs using different shutter times to accommodate different levels of incandescence resulted in overlap mismatch. These differences explain the wide range of density values reported in the literature[26] and collated in Figure 4. For levitated droplets, the average temperature dependence by Glorieux *et al.*[16] is weaker compared with our self-illumination data and slightly stronger compared with backlighting and their data show a higher degree of scatter (not shown in Fig. 4). The former can be related to the fact that the sample was imaged from the top and assumed to be spherical, which is clearly not the case (cf. Figure 3). Asphericity is also temperature dependent. The latter can be attributed to the tumbling motion of the sample in the nozzle which renders surface recognition difficult. However, calculating an error for our backlighting values taking into account a 5 μg (only balance, mass loss in short duration experiments negligible) uncertainty in sample weight and a 10 μm (about 4 pixel) uncertainty in sample radius represented by the error bar shown on the data point for the highest temperature clearly shows that within error bars our results agree with those of Glorieux.[16] The temperature dependence reported by Paradis *et al.*[33] is again stronger than for our work and densities deviate significantly. The reason could be camera resolution, which was lower in the work by Paradis,[33] sample evaporation since the work was carried out under high-vacuum conditions by Paradis,[33] and gas flow induced deformations in the lower part of the sphere hidden by the conical nozzle in our case. The much earlier measurements reported using conventional containment techniques by Kirshenbaum[48] might well have been affected by sample contamination and measurement uncertainties since the sample expansion was measured relative to the container. Taken together, the wide variation in density and expansion coefficient in the existing literature contrasts with the consistency of back lighted measurements described here. These show regularity across 1300° of temperature in the liquid state.

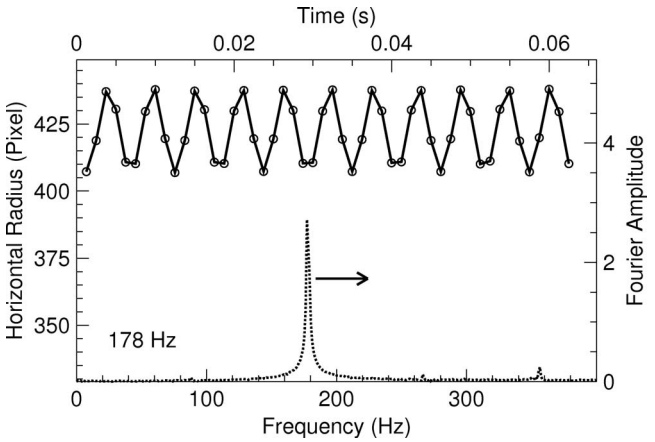

FIG. 5. First 50 data points of recorded horizontal droplet amplitude and Fourier amplitude of the entire recorded oscillation pattern (800 data points equaling 1 s recording time) for alumina at a droplet excitation frequency of 178 Hz at 2523 K.

In summary, our precise measurements (2% calculated error based on mass and radius uncertainties) of liquid density, which are correlated with the solid state thermal expansion coefficient and room temperature density, will enable cation and anion local environments to be more accurately refined. Furthermore, adopting shadow-casting with a high-power laser to high-pressure ESL work or modifying AL such that it works also with high-melting point materials may improve the accuracy of density measurements even further.

C. Surface tension

Because surface tension γ is related to the resonance frequency ν_R and mass M, the magnitude at a particular temperature is not affected by the imaging method. Acoustically driven excitation sweeps for alumina were conducted following procedures outlined in Sec. II D 1. An example is given in Figure 5 taken ~200° above the melting point of alumina. The oscillating horizontal droplet amplitude obtained from image analysis is shown together with the Fourier transform, where a fundamental resonance peak is clearly visible centered at 178 Hz with a small overtone at 356 Hz. This is compared to cuts of the Fourier spectra obtained from different excitation sweeps shown in Figure 6. Acoustic excitation of

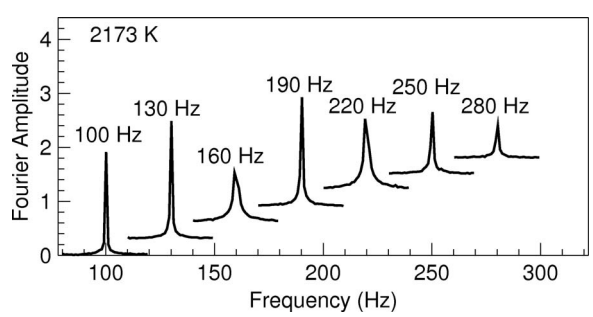

FIG. 6. Fourier amplitudes derived from the resonance scan for the horizontal amplitude of the droplet. Data are shown for different excitation frequencies of the oscillating sphere from 100 Hz to 280 Hz in steps of 30 Hz. The data were rescaled on the y-axis for clarity reasons adding 0.1 to each scan. Data are shown at each excitation frequency ±20 Hz.

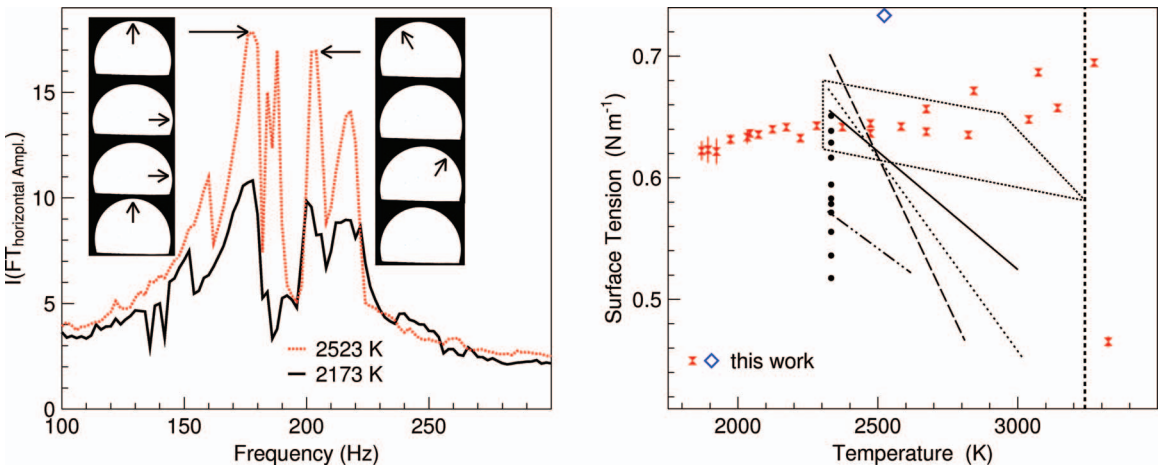

FIG. 7. (Left) Resonance scan using the driven damped harmonic oscillator method for a liquid alumina sphere at two different temperatures at 2523 K in the liquid and at 2173 K in the supercooled liquid state 150° below the melting point. (Right) Surface tension versus temperature obtained from Eq. (2) using values for the (l = 2, m = 0)-mode obtained from backlighting measurements. The area enclosed by the dotted line as well as all other lines represent data taken from the literature[41] with the enclosed area representing ADL data using incandescent imaging. The open diamond at 2523 K represents surface tension calculated using the sum rule[46] applied to the data from the left figure. The vertical dashed line represents the boiling point temperature of Al_2O_3.

liquid droplets clearly results in a clean oscillatory response at each frequency. Finally, the Fourier amplitudes of the entire frequency range are plotted in Figure 7 (left) for two different temperatures. These show a relatively clear pattern comprising five resonance peaks, the most prominent being at 178 Hz which can be attributed to the (l = 2, m = 0)-mode. A series of images, illustrating the alternating vertical and horizontal character of the mode, is shown alongside. The four peaks to the right can be identified with the rotationally split peaks of the (l = 2, m = ±1, ±2)-modes. The outer two peaks correspond to the (l = 2, m = ±2)-modes and the inner peaks to the (l = 0, m = ±1)-modes. Aerodynamically levitated droplets typically rotate at a frequency of a few Hz, which explains the splitting of the modes. The sample asphericity on the other hand accounts for their separation of the ($l = 2$, $m = 0$)-mode to the right. Surface tension values obtained from Eq. (2) are shown alongside in Figure 7. Since the levitated drop naturally adopts the (l = 2, m = 0)-mode when forced oscillations are switched off during damping experiments, these have also been added to Figure 7. Surface tension values are compared to earlier values from literature (Ref. 41 and references therein) which also reveal little or no temperature dependence. In all cases, Eq. (2) yields values around 0.65 N m^{-1}. Since only the (l = 2, m = 0)-mode is included, γ might well be underestimated by ∼20% (see discussion in Sec. II D 1) as indicated in Figure 7 (right) at 2573 K. Interesting to note is the sharp drop in surface tension as the boiling point is reached. Here, also the uncertainty in temperature measurement assuming a constant emissivity over the entire range becomes apparent.

D. Viscosity

Viscosity were obtained by acoustically exciting the sphere at its resonance frequency for the ($l = 2$, $m = 0$)-mode for several seconds and then switching off. The sample during forced oscillation and the decay were monitored by the high-speed camera running at 800 fps. The damping constant Γ and hence the viscosity η are obtained following the procedure outlined in Appendix D. Figure 8 shows viscosity results measured using shadow casting for molten and supercooled alumina as a function of temperature over the extended temperature range of ∼1400° between T_b and T_R, over which η increases by an order of magnitude. Error bars are calculated as standard deviations of the averaged data. Overall, our values obtained for alumina above the liquidus are consistent with earlier work on aerodynamically levitated alumina using sample self-excitation through the levitation gas and self-illumination at high temperatures close to T_b,[16] as well as in the vicinity of T_m.[42] The present data using backlighting and a well defined acoustic excitation, however, show substantially reduced scatter. They also extend throughout the supercooled range, rising considerably between melting (T_m)

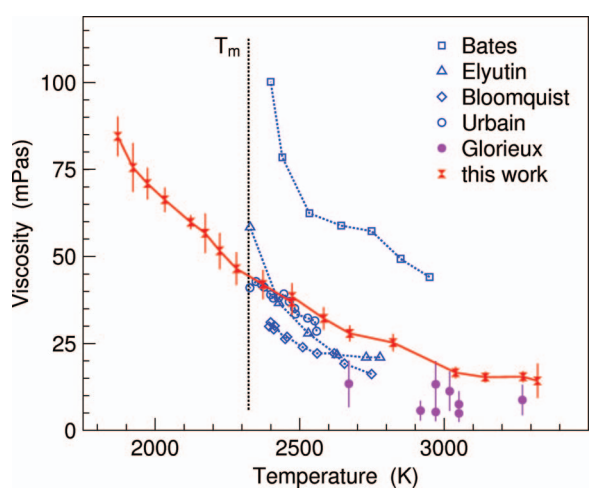

FIG. 8. Our viscosity data for alumina measured using shadow casting ADL (hourglass symbol), compared to literature data using self-illumination and conventional contacted techniques. Literature data were digitized from Glorieux *et al.*[16] using the same symbols. Additionally, the error bars estimated by Glorieux *et al.*[16] for their data are shown. Error bars for the present data are estimated to be about 20% of the measured value. The dashed line indicates the melting temperature of Al_2O_3.

and crystallization (T_R). Backlighting imaging enables the supercooled viscosity of alumina to be continuously related to rheology between melting and boiling. In particular, access to viscosity at supercooled temperatures, which our work enables, will inform the solidification processes that accompany recalescence.

Taken together, while viscosity values measured using ADL are reasonably consistent, they deviate substantially from previously reported data obtained by classical viscosity methods.[42,49–51] It is likely these differences between contactless and contacted measurements may well be affected by the interaction between molten alumina and the container, and wetting behavior in the latter case.

IV. CONCLUSION

A compact novel aerodynamic levitation facility has been developed that enables to reliably measure the thermophysical properties of high temperature liquids. By employing two lasers, temperature gradients across the specimen are minimized. Droplet oscillations are realized in a controlled way by incorporating acoustic excitation via the levitating gas. Imaged using a high-speed camera, accurate measurements of surface tension, viscosity, and density are obtained and demonstrated using liquid alumina as a test case. A comparison with previously obtained data shows that for accurate density determination both, the horizontal and the vertical radii of the levitated sample have to be determined. Moreover, shadow casting is critical to obtain reliable calibrated values of droplet shape and size over extensive temperature ranges. In future, the facility will be further developed for routinely measuring thermophysical properties of high temperature liquids *in situ* in conjunction with structure factor determination using synchrotron radiation and neutron sources.

ACKNOWLEDGMENTS

We are grateful to R. Winter for providing us with a second CO_2 laser. We thank L. Hennet at CNRS-CEMHTI, Orleans, France, for advice on levitation technology. We thank the German Academic Exchange Service (DAAD) for part-funding of the stay of G. N. Greaves at the DLR. We thank J. Brillo for reading of the paper and valuable comments to it. We also acknowledge the support of the Higher Education Funding Council of Wales (HEFCW) through the Centre for Advanced Functional Materials and Devices (CAFMaD).

APPENDIX A: SAMPLE MATERIAL

Ruby spheres of 2 mm diameter (Precision Ball & Gauge Co Grade 25 and Oskar Moser Grade 20) were used for the equipment characterization experiments and as the source for liquid alumina. A pristine polished ruby sphere was used for each heating and cooling cycle. The liquid droplet was soaked at 2700 K for 10 min to remove the chromium oxide content as verified by atomic absorption spectroscopy of processed samples in agreement with reports in literature.[52] Polished single phase solids levitate well and enable density to be measured between ambient and melting temperatures. Another reason for using pristine spheres is shrinkage-hole formation on solidification of a melted sphere which leads to bubbles being trapped inside the sphere upon remelting. The spheres were checked for their weight before and after each experiment on a balance with an accuracy of 5 μg. Typically, the ruby spheres lost about 0.1 mg for various length of an experiment, increasing to ~1 mg as the boiling point was reached.

TABLE I. Gauge sphere nominal diameters (ND), measured diameters in pixel (R_H horizontal and R_V vertical), and calculated effective pixel size.

Type	ND (mm)	R_H	R_V	EPS (μm/pixel)
Steel	2.000	381.0	381.5	2.620
Steel	2.381	451.5	452.0	2.635
Steel	2.500	473.0	472.5	2.646
Ruby	2.000	379.0	380.0	2.635

APPENDIX B: CAMERA CALIBRATION

Nominal per pixel resolution achieved with the combination of camera and lens is 2.8 μm for the MotionBlitz camera. For calibration precision milled steel ball bearings 2 mm, 2.381 mm, and 2.5 mm (SKF) and 2 mm ruby spheres (Grade 20) were used. The back lighted sphere was recorded and its radius in pixels was determined through sample surface recognition, verifying the nominal pixel resolution. Values obtained for the diameters of the different spheres are listed in Table I. The data clearly show that the effective pixel size (EPS) depends slightly on the radius of the sphere. This is in line with the tabulated lens distortion.

APPENDIX C: IMAGE ANALYSIS METHODS

Owing to the configuration of the aerodynamic levitator a portion of the bottom of the droplet remains in the nozzle, hence the image processing software has to interpolate the shape of the droplet from the visible portion (Figure 9). The

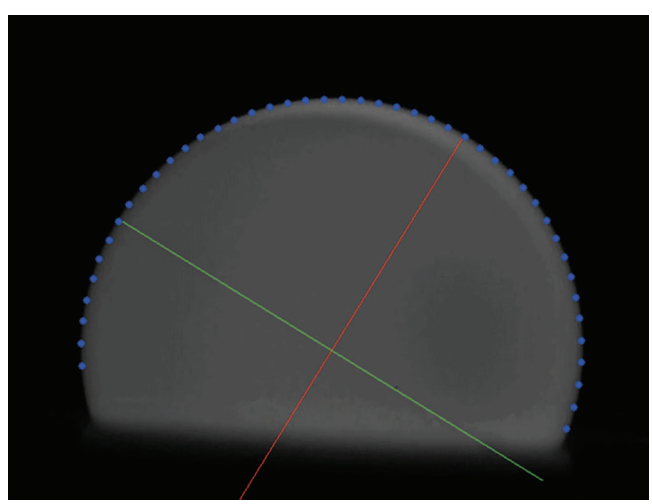

FIG. 9. Typical frame from high speed camera showing portion of sample visible above levitation nozzle. Also shown are points found by edge detection routine (blue) together with the major-axis (red) and minor-axis (green) of the ellipse fitted through points.

image processing pipeline written in LabView makes extensive use of the NI Vision library routines. The operator uses the first frame of the recorded video to manually select an annular region of interest containing the approximate location of the visible portion of the edge of the droplet. Once the annular region is defined, processing takes place on the rest of the frames in the video using the same parameters. A spoke detection algorithm automatically detects the edge of the droplet along radial lines from the center of the annulus at 5° intervals, giving approximately 45 points for a typical droplet. An ellipse fit algorithm is then used to reconstruct the elliptical projection of the droplet and find the center point together with locations of the major and minor axes and the projected area of the ellipse. From these parameters, the width and height of the droplet are also calculated. All the ellipse parameters are saved for each frame in the video. A Fourier transform is then used to obtain a power spectrum from the horizontal and vertical radii components of the ellipse parameters.

APPENDIX D: VISCOSITY ANALYSIS

A sine function (cf. Eq. (4)) is fitted to the part of the recorded curve [cf. Figure 10(b)] where the sample is acoustically excited. From this the resonance amplitude A and the offset time t_0 are determined, which are fixed for fitting of the damped-harmonic oscillator equation (cf. Eq. (5)) to the decay data. The decay data are fitted with four free parameters: the resonance frequency ν_{dho}, the average sample radius R_{av}, the start time of the decay t_1, and the decay constant Γ. Γ and t_1 appear to be correlated. In order to obtain the best fit, t_1 has to be chosen sufficiently close to its real value. All of the determined radii in horizontal and vertical direction are analyzed. The frequencies determined from the harmonic oscillator and the decay data fit are typically slightly different if the forced oscillator frequency is slightly different from the primary resonant frequency ($l = 2$, $m = 0$). Hereby, the droplet oscillation frequency almost instantaneously shifts to the primary resonance frequency at the start of the decay.

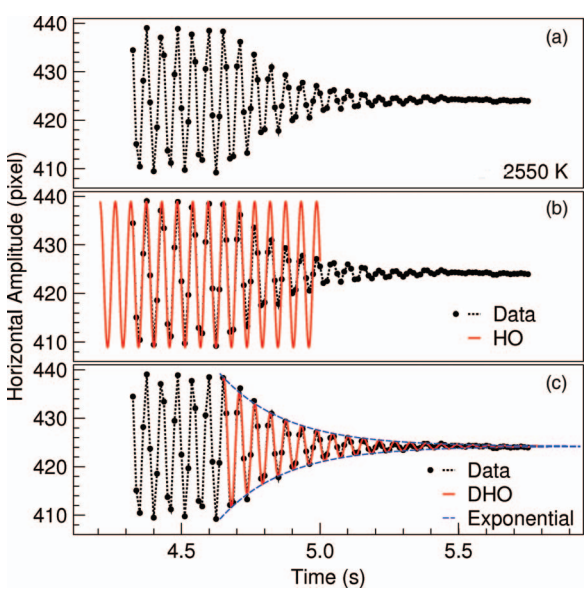

FIG. 10. Damping curve of horizontal sample radius (a), harmonic oscillator (b), and damped harmonic oscillator fit (c) to the recorded radius data, respectively.

TABLE II. Fit parameters for the horizontal radii as resulting from the harmonic oscillator fit to the excitation part and the damped harmonic oscillator fit to the decay part of the recorded amplitudes.

T (K)	A (pixel)	ν_{ho} (Hz)	ν_{dho} (Hz)	R_{av} (pixel)	Γ (s^{-1})
1870	4.1	180.0	178.3	423	117
1923	6.1	180.0	178.3	425	105
1973	6.7	180.0	179.8	426	98.9
2033	7.3	180.0	179.7	427	92.2
2123	6.4	180.0	180.9	423	82.7
2173	9.5	180.0	181.2	426	79.1
2223	7.4	180.0	179.8	423	71.4
2281	11.5	180.0	180.9	427	64.9
2373	12.9	180.0	180.8	428	58.6
2473	9.5	180.0	180.5	424	51.2
2583	16.6	180.0	181.1	428	45.0
2673	13.4	180.0	183.3	419	35.2
2823	21.0	180.0	180.4	429	35.5
3039	21.5	180.0	182.7	422	23.1
3142	19.6	180.0	185.0	416	21.2
3273	8.0	180.0	193.0	401	21.3
3323	3.1	168.0	163.1	403	21.0

Table II summarizes the fit parameters A, R_{av}, Γ, and ν_{dho} of the damped harmonic oscillator fit as well as the excitation frequency ν_{ho} of the harmonic oscillator fit to the horizontal radii for different temperatures.

[1] I. Egry, G. Lohöfer, and S. Sauerland, Int. J. Thermophys. **14**, 573 (1993).
[2] J. Brillo and I. Egry, Int. J. Thermophys. **24**, 1155 (2003).
[3] I. Egry, H. Giffard, and S. Schneider, Meas. Sci. Technol. **16**, 426 (2005).
[4] J. Brillo and I. Egry, Jpn. J. Appl. Phys. **50**, 11RD02 (2011).
[5] G. Lohöfer and G. Pottlacher, High Temp. - High Press. **40**, 237 (2011).
[6] W.-K. Rhim, S. K. Chung, D. Barber, K. F. Man, G. Gutt, A. Rulison, and R. E. Spjutb, Rev. Sci. Instrum. **64**, 2961 (1993).
[7] K. Ohsaka, S. K. Chung, W.-K. Rhim, and J. C. Holzer, Appl. Phys. Lett. **70**, 423 (1997).
[8] W.-K. Rhim, K. Ohsaka, P.-F. Paradis, and R. E. Spjutb, Rev. Sci. Instrum. **70**, 2796 (1999).
[9] M. Papoular and C. Parayre, Phys. Rev. Lett. **78**, 2120 (1997).
[10] J. C. Barbe, C. Parayre, M. Daniel, M. Papoular, and N. Kernevez, Int. J. Thermophys. **20**, 1071 (1999).
[11] P. H. Haumesser, J. Bancillon, M. Daniel, M. Perez, and J. P. Garandet, Rev. Sci. Instrum. **73**, 3275 (2002).
[12] E. H. Trinh and K. Ohsaka, Int. J. Thermophys. **16**, 545 (1995).
[13] Y. Bayazitoglu and G. Mitchell, J. Thermophys. Heat Transfer **9**, 694 (1995).
[14] G. F. Mitchell, Y. Bayazitoglu, and R. Shampine, J. Thermophys. Heat Transfer **12**, 599 (1998).
[15] K. Ohsaka, A. Rednikov, S. S. Sadhal, and E. H. Trinh, Rev. Sci. Instrum. **73**, 2091 (2002).
[16] B. Glorieux, M.-L. Saboungi, F. Millot, J. Enderby, and J.-C. Rifflet, AIP Conf. Proc. **552**, 316 (2001).
[17] B. Coté, D. Massiot, F. Taulelle, and J. P. Coutures, Chem. Geol. **96**, 367 (1992).
[18] S. Ansell, S. Krishnan, J. K. R. Weber, J. J. Felten, P. C. Nordine, M. A. Beno, D. L. Price, and M. L. Saboungi, Phys. Rev. Lett. **78**, 464 (1997).
[19] L. Landron, L. Hennet, J. P. Coutures, T. E. Jenkins, C. Aletru, G. N. Greaves, A. Soper, and G. E. Derbyshire, Rev. Sci. Instrum. **71**, 1745 (2000).
[20] C. Landron, L. Hennet, T. E. Jenkins, G. N. Greaves, J. P. Coutures, and A. K. Soper, Phys. Rev. Lett. **86**, 4839 (2001).
[21] H. Sinn, B. Glorieux, L. Hennet, A. Alatas, M. Hu, E. E. Alp, F. J. Bermejo, D. L. Price, and M. L. Saboungi, Science **299**, 2047 (2003).

[22]L. Hennet, I. Pozdnyakova, V. Cristiglio, S. Krishnan, A. Bytchkov, F. Albergamo, G. J. Cuello, J.-F. Brun, H. E. Fischer, D. Zanghi, S. Brassamin, M. L. Saboungi, and D. L. Price, J. Non-Cryst. Solids **353**, 1705 (2007).
[23]G. N. Greaves, M. C. Wilding, S. Fearn, D. Langstaff, F. Kargl, S. Cox, O. Majerús, Q. Vu Van, C. J. Benmore, R. Weber, C. M. Martin, and L. Hennet, Science **322**, 566 (2008).
[24]J. Kozaily, L. Hennet, H. E. Fischer, M. M. Koza, S. Brassamin, S. Magazu, and F. Kargl, Phys. Status Solidi C **8**, 3155 (2011).
[25]D. D. Qu, A. Mizuno, M. Watanabe, J. Bednarcik, and J. Shen, Mater. Sci. Eng. A **555**, 36 (2012).
[26]L. B. Skinner, A. C. Barnes, P. S. Salmon, L. Hennet, H. Fischer, C. J. Benmore, S. Kohara, J. K. R. Weber, A. Bytchkov, M. C. Wilding, J. B. Parise, T. O. Farmer, I. Pozdnyakova, S. K. Tumber, and K. Ohara, Phys. Rev. B **87**, 024201 (2013).
[27]G. N. Greaves and S. Sen, Adv. Phys. **56**, 1 (2007).
[28]I. Egry, G. Lohöfer, I. Seyhan, S. Schneider, and B. Feuerbacher, Appl. Phys. Lett. **73**, 462 (1998).
[29]I. Egry, G. Lohöfer, S. Schneider, I. Seyhan, and B. Feuerbacher, *Solidification*, edited by W. H. Hofmeister, J. R. Rogers, N. B. Singh, S. P. Marsh, P. W. Vorhees (1999), p. 15–22.
[30]V. Bojarevics and K. Pericleous, ISIJ Int. **43**, 890 (2003).
[31]J. Etay, P. Schetelat, B. Bardet, J. Priede, V. Bojarevics, and K. Pericleous, High Temp. Mater. Processes (N.Y., NY, U.S.) **27**, 439 (2008).
[32]K. J. Cheng, Phys. Lett. **112A**, 392 (1985).
[33]P. F. Paradis, T. Ishikawa, Y. Saito, and S. Yoda, Jpn. J. Appl. Phys. **43**, 1496 (2004).
[34]P. F. Paradis and T. Ishikawa, Jpn. J. Appl. Phys. **44**, 5082 (2005).
[35]T. Ishikawa, J. Yu, and P. F. Paradis, Rev. Sci. Instrum. **77**, 053901 (2006).
[36]Y. Yamamoto, Y. Abe, A. Fujiwara, K. Hasegawa, and K. Aoki, Microgravity Sci. Technol. **20**, 277 (2008).
[37]P. F. Paradis, F. Babin, and J. M. Gagne, Rev. Sci. Instrum. **67**, 262 (1996).
[38]S. Krishnan, J. J. Felten, J. E. Rix, J. K. R. Weber, P. C. Nordine, M. A. Beno, S. Ansell, and D. L. Price, Rev. Sci. Instrum. **68**, 3512 (1997).
[39]J. K. R. Weber, J. G. Abadie, A. D. Hixson, P. C. Nordine, and G. A. Jerman, J. Am. Ceram. Soc. **83**, 1868 (2000).
[40]L. Hennet, I. Pozdnyakova, A. Bytchkov, V. Cristiglio, P. Palleau, H. E. Fischer, G. J. Cuello, M. Johnson, P. Melin, D. Zanghi, S. Brassamin, J. F. Brun, D. L. Price, and M. L. Saboungi, Rev. Sci. Instrum. **77**, 053903 (2006).
[41]B. Glorieux, F. Millot, and J. C. Rifflet, Int. J. Thermophys. **23**, 1249 (2002).
[42]G. Urbain, Rev. Int. Hautes Temp. Refract. **19**, 55 (1982).
[43]R. K. Wunderlich, H.-J. Fecht, I. Egry, J. Etay, L. Battezzati, E. Ricci, T. Matsushita, and S. Seetharaman, J. Iron Steel Res. Int. **83**, 43 (2012).
[44]Lord Rayleigh, Proc. R. Soc. London **29**, 71 (1879).
[45]F. H. Busse, J. Fluid Mech. **142**, 1 (1984).
[46]D. L. Cummings and D. A. Blackburn, J. Fluid Mech. **224**, 395 (1991).
[47]H. Lamb, Proc. London Math. Soc. **s1-13**, 51 (1881).
[48]A. D. Kirshenbaum and J. A. Cahill, J. Inorg. Nucl. Chem. **14**, 283 (1960).
[49]J. L. Bates, C. E. Mc Neilly, and J. J. Rasmussen, in *Ceramics in Severe Environments, Material Science Research*, edited by W. W. Kriegel and H. Palmour III (Plenum Press, New York, 1971), Vol. 5, p. 111.
[50]V. P. Elyutin, B. C. Mitin, and Y. A. Nagibin, Fiz. Aerodispersnykh Sist. **7**, 104 (1972).
[51]R. A. Blomquist, J. K. Fink, and L. Leibowitz, Ceram. Bull. **5**, 522 (1978).
[52]A. B. Biswas, J. K. R. Weber, and P. C. Nordine, J. Mater. Res. **10**, 1823 (1995).